Photoacoustic dose monitoring in clinical high-energy photon beams

Olivia M. Giza[1,2], Daniel Sánchez-Parcerisa[1,2]*, Víctor Sánchez-Tembleque[1,2], Joaquin L. Herraiz[1,2], Jorge Camacho[3], Stephen Avery[4], José Manuel Udías[1,2]

[1] Grupo de Física Nuclear & IPARCOS, Departamento de Estructura de la Materia, Física Térmica y Electrónica, Universidad Complutense de Madrid, CEI Moncloa, 28040 Madrid, Spain.

[2] Instituto de Investigación Sanitaria del Hospital Clínico San Carlos (IdISSC), Madrid, Spain

[3] ITEFI, Spanish National Research Council (CSIC), Madrid, Spain.

[4] Department of Radiation Oncology, Hospital of the University of Pennsylvania, Philadelphia, PA 19104, USA.

*Corresponding author: dsparcerisa@ucm.es

Abstract

This work describes all stages of development (setup, optimization, performance, and first experimental measurements) of an acoustic sensor that can be used for range monitoring and dosimetry of clinical radiotherapy beams.

The detection device consists of an ultrasonic transducer, a combination of preamplifiers and differential amplifiers with filtered outputs and a digital oscilloscope. Simulations of the experimental setup were carried out to study the optimal measurement geometry and choice of transducer. The dose distributions were calculated with the Monte Carlo code FLUKA, while the acoustic simulations were performed with the analytical wave transport code k-Wave. The temporal profiles of the dose pulses, in the order of μs, were measured with a scintillating crystal coupled to a photomultiplier and used as input for the acoustic simulation. Measurements were performed in a Cyberknife™ radiosurgery beam and a TrueBeam unit. A lead block was submerged in water and placed partially or totally in the irradiation field in order to increase the acoustic signal.

Photoacoustic signals were detected with both beams with the expected shape and time-delay, after the frequency response of the detection system was taken into account. The proposed setup can detect photoacoustic signals originating from the penumbra of the treatment fields after being processed with the appropriate image analysis tools.

1. Introduction

When a certain amount of energy is deposited in a target material by a radiation field, the temperature in the material increases locally, causing a thermoelastic expansion. As a consequence of this expansion, a pressure wave is generated. This is known as the radiation-induced thermoacoustic effect (Sulak *et al* 1979). The amplitude of this acoustic signal is proportional to the energy deposited by the radiation (Sieger & Lefebre 1985), and the properties of the wave depend on the geometrical and temporal energy distributions of the radiation field.

Several applications of the thermoacoustic effect have been proposed in medical physics (Hickling et al 2018b), from photoacoustic imaging with non-ionizing laser (Beard 2011) and gamma-ray beams (Xiang *et al* 2013a, 2013b), to dosimetry and beam localization for clinical high-energy photon beams (Sampaio *et al* 2015, Kim *et al* 2017, Hickling *et al* 2017). Indeed, a combination of radiation-induced thermoacoustic effect and computed tomography, named X-Ray Acoustic CT (XACT), has gained considerable attention in recent years, going from simulation studies (Hickling *et al* 2014b) to undergo tests in clinical facilities under different configurations (Xiang et al 2013b, Hickling *et al* 2017, 2018a, Lei *et al* 2018).

To solve the well-known problem of range uncertainties in particle radiotherapy (Paganetti 2012), systems based on protoacoustic (or ionoacoustic) effects have recently been proposed (Parodi & Assmann 2015). While the first experimental measurements of the protoacoustic effect were carried out decades ago (Sulak *et al* 1979, Hayakawa *et al* 1995, Albul *et al* 2001), recent works including simulation studies (Jones *et al* 2014, 2016a, 2018, Alsanea *et al* 2015, Kipergil *et al* 2017) and experimental data taken at proton facilities (Jones *et al* 2015, 2016b, Assmann *et al* 2015, Lehrack *et al* 2017, Nie *et al* 2018, Patch *et al* 2019) have significantly contributed to the possibility that such a system would achieve clinical maturity in the near future.

The development of clinical devices for dosimetry or range verification based on the radiation-induced thermoacoustic effect faces several technical difficulties. First and most importantly, the measurable acoustic signals are extremely weak. The predicted intensity of the pressure wave depends on the temporal and geometrical properties of the deposited dose distribution, in the few mPa range for a detector placed a ~10 cm away from a clinical proton field in the μs range (Jones *et al* 2015, Kipergil *et al* 2017). This problem is aggravated by the presence of strong electromagnetic fields around medical accelerators, interfering with sensitive ultrasound equipment and limiting the achievable signal-to-noise ratio (SNR).

Reconstruction of dose distribution from the detected waves is challenging due to the uncertainties in tissue composition (Fontanarosa et al 2011, Alsanea et al 2015) and the low SNR. For this reason, developing an accurate simulation package is vital not only for improving and understanding the experimental setup, but also to test and optimize the image reconstruction procedure. In previous works, acoustic simulations based on the wave propagator *k-Wave* (Treeby et al 2010) have been able to reproduce the arrival time of the signals but have failed to accurately describe the shape of the acoustic waves, due to noise, uncertainties in material properties, and detector response. Only recently the work of Nie *et al* (2018) has shown good progress in describing full waveforms for certain homogeneous materials.

Finally, pulse characteristics of beams are also a strong limiting factor for the usability of these systems, since only pulsed beams with a duration of the order of a few μs (or less) fulfill the 'stress confinement' condition, necessary for accurate protoacoustic range determination (Ahmad *et al* 2015, Jones *et al* 2016a). Only synchrotrons and modern synchrocyclotrons have such a short pulse duration while, according to PTCOG statistics (2018), most centers are based on isochronous cyclotrons, which need additional hardware to produce short pulses (Jones *et al* 2015). Therefore, with only a few particle centers currently able to produce beams suitable for protoacoustic verification, the development and testing of such detection systems can be partially carried out in standard photon LINACs, with a μs-pulse duration, since the properties of the produced acoustic wave are relatively independent on the radiation type.

In this work we present an experimental device composed of a large-bandwidth ultrasound transducer and a set of amplification electronics which is optimized for dosimetry and range verification of clinical radiation fields. Using lead blocks to amplify the signal (Xiang et al 2013b, Hickling et al 2014a), we tested our device successfully in two different clinical photon beams. The information gathered in these initial experiments has been used to develop a simulation package that can be easily adapted to other experimental setups.

2. Materials and methods

Using computational simulations and experimental measurements, we investigated pressure waves created upon irradiation of a water tank with a 6×10 cm^2, 6 MV-photon beam from a TrueBeam™ linear accelerator (Varian Medical Systems, Palo Alto, CA) and with a 4-cm diameter, 6 MV radiosurgery beam from a Cyberknife™ unit (Accuray Inc., Sunnyvale, CA). A lead block with dimensions $4 \times 8 \times 2.5$ cm^3 was submerged in the water tank and placed in the center of the irradiation field with its broad face pointed at the transducer, which was placed at a varying distance d between 1.5 and 10 cm from edge of the lead block (see Figure 1).

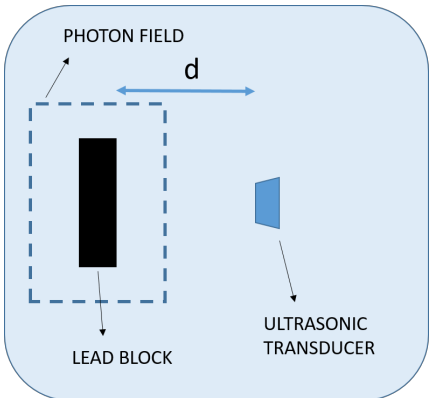

Figure 1. Scheme of the experimental setup. Photon field enters perpendicular to the paper. Distance *d* varies between 1.5 and 10 cm.

2.1. Radiation-induced thermoacoustic effect

Energy deposition from a radiation source causes a heating of the target material in the order of μK, which in turn produces an expansion, generating an acoustic pressure wave (in the order of mPa). The local pressure increase p_{source} (originated from the instantaneous dose deposition, i.e. before propagation in the medium) is proportional to the deposited dose D, the density of the material ρ and the Grüneisen coefficient Γ of the medium (Lyamshev, 2004):

$$p_{source}(\vec{r},t) = \Gamma(\vec{r}) \cdot \rho(\vec{r}) \cdot D(\vec{r},t), \tag{1}$$

where the Grüneisen coefficient depends on the speed of sound in the material (v_s) and its heat capacity (C_p) and volume thermal expansion coefficient (α),

$$\Gamma = \frac{v_s^2 \cdot \alpha}{C_p}. \tag{2}$$

The dose deposited in the medium, $D(\vec{r},t)$, can be separated in two components which can be studied individually: the spatial dose distribution and the time distribution properties of the dose pulse (Jones *et al*, 2014):

$$D(\vec{r},t) = D(\vec{r}) \cdot D(t). \tag{3}$$

The general wave equation describes how the local pressure $p_{source}(\vec{r},t)$ propagates across a medium, $p(\vec{r},t)$:

$$\nabla^2 p(\vec{r},t) - \frac{1}{v_s^2} \cdot \frac{\partial^2 p(\vec{r},t)}{dt^2} = -\frac{1}{v_s^2} \cdot \frac{\partial p_{source}(\vec{r},t)}{dt}, \tag{4}$$

2.2. *Gamma-acoustic simulation*

In this work, Monte Carlo particle transport and analytical photoacoustic simulation techniques were combined to develop a simulation workflow capable of modeling the induction of acoustic waves following irradiation and their subsequent propagation in the lead+water setup.

The physical properties of lead and water (Haynes 2014) used in the simulations are displayed in Table 1. The absorption coefficient of lead (α_p) due to the lack of a reference value, was derived by comparison to similar metals. A sensitivity study (Giza 2017) was conducted, concluding that this estimation does not affect the results of the simulation, where values of α_p between 0.5 and 20 dB/MHz^2·cm produced variations of simulated pressure of less than 4 % and no appreciable difference in the arrival time of the signal.

Table 1. Physical properties of lead and water used in the simulations. Source: (Haynes 2014).

Material	**Water at 22 ºC**	**Lead**
Density (kg/m^3)	997.75	11350
Compressional wave speed (m/s)	1488	2160
Shear wave speed (m/s)	0	700
Grüneisen coefficient, Γ	0.11	3.12
Compressional wave absorption, α_p (dB/MHz^2·cm)	0.0022	8.686
Pressure-Dose relation (eq. 1)	0.11 Pa / mGy	35.412 Pa / mGy

The spatial dose distributions in the lead+water geometry, $D(\vec{r})$, were calculated with Monte Carlo code *FLUKA* (Ferrari et al 2005, Böhlen et al 2014) for both linear accelerators. For simplicity reasons, in both cases the complex energy spectrum of the 6 MV photon beam was approximated by a monoenergetic beam of 2 MeV. This approach has been used by other authors (Hickling et al 2014a) and was validated by a previous study (Giza 2017), where no relevant differences were found on the pulse shape or arrival times of signals induced by monoenergetic photon beams in the 0.5– 6 MeV energy range.

Dose was scored in FLUKA using the USRBIN scorer in a Cartesian grid with 1-mm^3 side cubic voxels for the entire region of interest, corresponding to the water tank. Each simulation comprised 10^6 stories, divided into five cycles of 200,000 primary particles. The average simulation time of each run was approximately 10 minutes on a workstation with 4 quad-core 2.4 GHz processors and 42 GB of RAM memory.

The temporal profiles of the dose pulses, $D(t)$, were measured using photomultiplier tubes (PMT) coupled with plastic and $CeBr_3$ scintillators, respectively, for the TrueBeam and Cyberknife units. Both pulses are shown in Figure 2. The specifics of these measurements are described elsewhere (Jones et al 2014, Sánchez-Tembleque et al 2018).

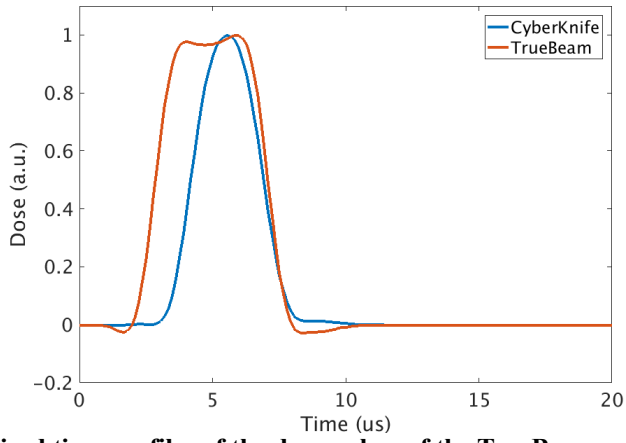

Figure 2. Normalized time profiles of the dose pulses of the TrueBeam and CyberKnife units. Curves are filtered with a low-pass filter (maximum frequency depends on the size of the simulation grid).

These $D(\vec{r})$ and $D(t)$ distributions were used as inputs for the analytical wave transport code *k-Wave*, a MATLAB toolbox for the propagation of acoustic waves in the time domain (Treeby et al 2010). We used a three-dimensional geometry, with a grid of 200×200×400 1-mm^3 voxels and physical properties of lead and water as described in Table 1. The simulations were performed with the pstdElastic3D function of k-Wave, which simulates the propagation of compressional and shear waves in isotropic elastic and viscoelastic media using a method based on the pseudospectral time domain (PSTD) method. Although the detector is immersed in water (a fluid medium), the conversion between different wave modes in the lead+water interface makes it necessary to use elastic simulation method for full accuracy and despite their higher computational cost.

From $p(\vec{r},t)$, the simulated pressure distribution calculated with k-Wave, we estimated the expected signal *S(t)* measured by the transducer. Let T represent the set of n_T points in space conforming the transducer, then *S(t)* is calculated as the average pressure at all voxels defined as part of the transducer:

$$S(t) = \frac{\sum_{\vec{r}\in T} p(\vec{r},t)}{n_T} \quad (5)$$

For the initial calculation of S(t), *T* was represented by a disc with a diameter of 3 cm and a flat response in the frequency domain. The estimated frequency response of the transducer and the amplification system was added in the data analysis stage as *a posteriori* information from the experimental measurements, as described in section 3.3.

2.3. Description of the experimental setup

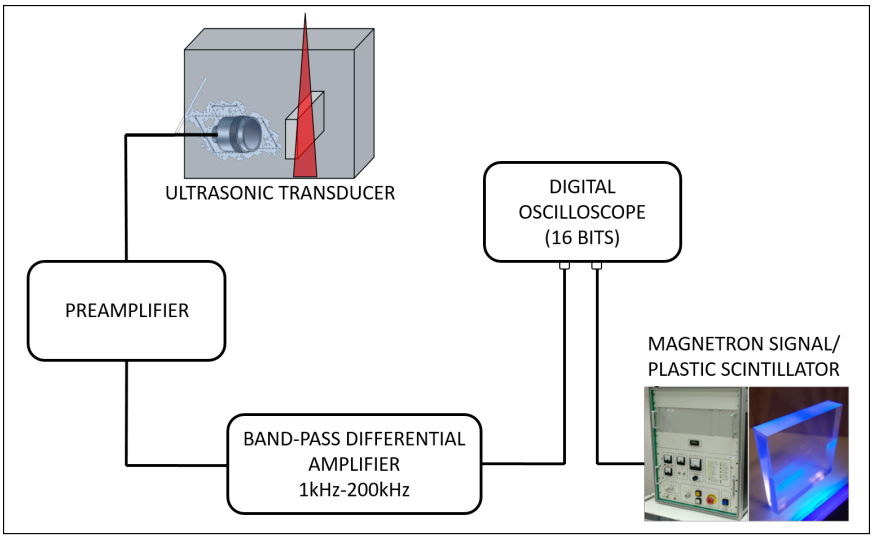

Figure 3. Sketch of the ultrasonic signal acquisition system

The experimental setup, depicted in Figure 3, consists of an ultrasonic transducer, a combination of preamplifiers and differential amplifiers with filtered outputs, and a digital oscilloscope. The transducer was a custom-built device with a diameter of 30 mm, a central frequency of 300 kHz and a bandwidth of 40%. The preamplifier was a Dasel Amplus-32 (Dasel Sistemas, Madrid, Spain) with a bandwidth of 30kHz – 1MHz and a gain of 32 dB. The signal from the preamplifier was further amplified using a differential amplifier Alligator USBPBP-S1 (Alligator Technologies, Costa Mesa, CA) with a band-pass filter between 1kHz and 200kHz and a maximum gain of 30 dB.

The digitalization of the signal was performed with a 16-bit digital oscilloscope (PicoScope 4262), connected to a control computer via USB. Copper foil was wrapped around all devices for electromagnetic shielding, to minimize interference with the strong electromagnetic fields present in the treatment rooms. Before irradiation, the water in the tank was left to thermalize for over two hours, for a standard room temperature of 22 ºC.

The TrueBeam™ measurements were carried out at the Hospital of the University of Pennsylvania (Philadelphia, PA). Beam energy was selected at 6 MV, and the beam collimator was used to shape a 10 × 6 cm^2 field, irradiating the full contour of the lead block plus a 1-cm margin, measured directly on the lead block plane, placed at the isocenter. Flattening filter mode was used, with a dose rate of 600 MU/min and a pulse repetition frequency of 360 Hz, which yields a maximum dose per pulse of 0.28 mGy with a duration of 6 µs (red line in Figure 2). The acquisition was triggered by scattered prompt gammas arriving at a plastic scintillator coupled with a PMT. Measurements were performed at lead block to transducer distances of 24, 58 and 100 mm.

The Cyberknife™ measurements were performed at Hospital Ruber Internacional (Madrid, Spain). A circular brass collimator with an aperture size of 40 mm at isocenter (reference source-axis distance of 80 cm) was used to shape the field. Since the surface of the water tank was placed at a distance of 60 cm from the collimator, the projected size of the photon field at the surface of the lead block was 3 cm. The dose pulse is approximately square, with a duration of about 5 µs (blue line in Figure 2) and a pulse repetition frequency of 188 Hz. The dose rate was kept at 600 MU/min for a maximum dose per pulse of 0.53 mGy. Lead block to transducer

distances used were 15, 55 and 80 mm. In this case, the acquisition was triggered using the magnetron output signal (MAG) from the Cyberknife™ control unit. This signal is active whenever the high-voltage magnets are energized, regardless of whether the beam is on or not, which allowed us to use the same trigger signal to acquire "dry" runs, used for background subtraction measurements (see Figure 4).

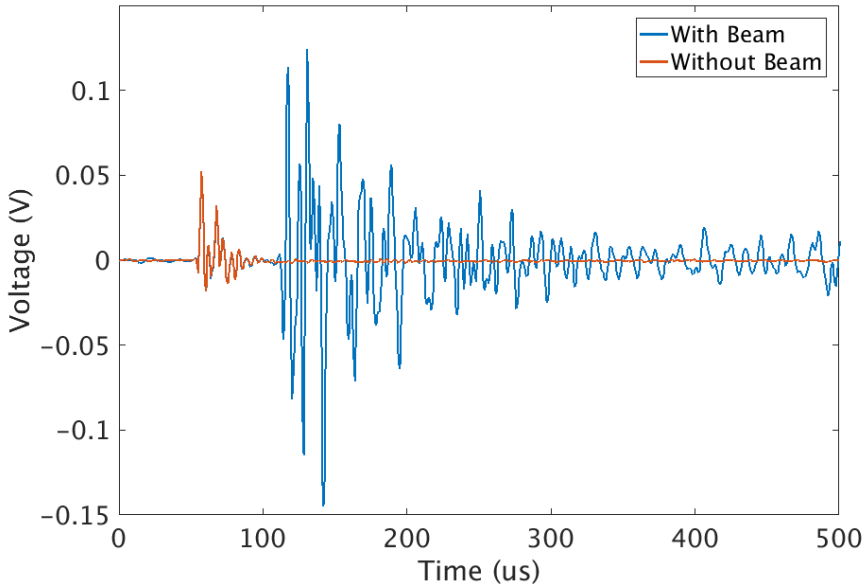

Figure 4. Acoustic signals measured at the Cyberknife™ unit with a lead block to transducer distance of 80 mm, with radiofrequency signal on but no beam (red curve, background signal) and with beam on (blue curve).

For each measurement, a batch of 1024 consecutive traces was obtained (in less than 10 s) and averaged in order to reduce the effect of random electromagnetic noise in the acquired signals. With this setup, signal-to-noise ratios in the order of 250 were obtained (taking into account only random noise).

3. Results

3.1. Measurement of the electronic delay.

For all the measurements in each batch, trigger signals were co-registered along with transducer measurements and used to synchronize the measured time profiles at the trigger threshold level. Moreover, the measured signals were affected by an electronic delay originating from the amplification hardware. To ascertain the value of the delay, signal arrival times for all signals were derived (setting the arrival time when the wave crossed 50% of the value for the first peak) and plotted against the lead block to transducer distance. The slope of the curve was fixed at the value of sound speed in water (Table 1), thus the intersection with the y-axis corresponded to the time lag in the experimental measurements. Due to the small number of detection points and high uncertainty in arrival times caused by electromagnetic noise, we decided to fix the slope of the fit to that of the speed of sound in water to obtain an accurate and consistent estimation on the electronic delay. As displayed in Figure 5, the electronic delay was similar for both measurement setups: (11.9 ± 0.5) μs for the TrueBeam and (12.1 ± 0.9) μs for the Cyberknife.

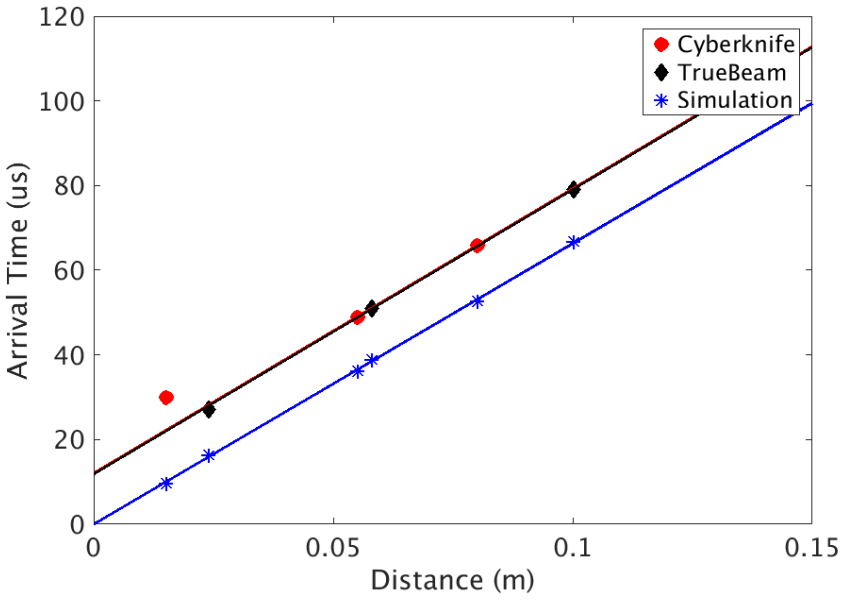

Figure 5. Signal arrival time VS lead block to transducer distance plots, used to determine the electronic delay of the amplification system.

3.2. Measured acoustic signals

After applying corrections for trigger position and electronic delay, measured signals are shown in Figures 6 and 7 for the Truebeam and Cyberknife accelerators respectively, together with the simulations carried out as explained in Section 2.1. For lead block to transducer distances above 55 mm, signal arrival time and first pulse duration are in agreement with the simulated waves. For shorter distances, as observed by other authors (Hickling et al 2014a), unfiltered electromagnetic noise and reflected waves distort the shape of the pulses.

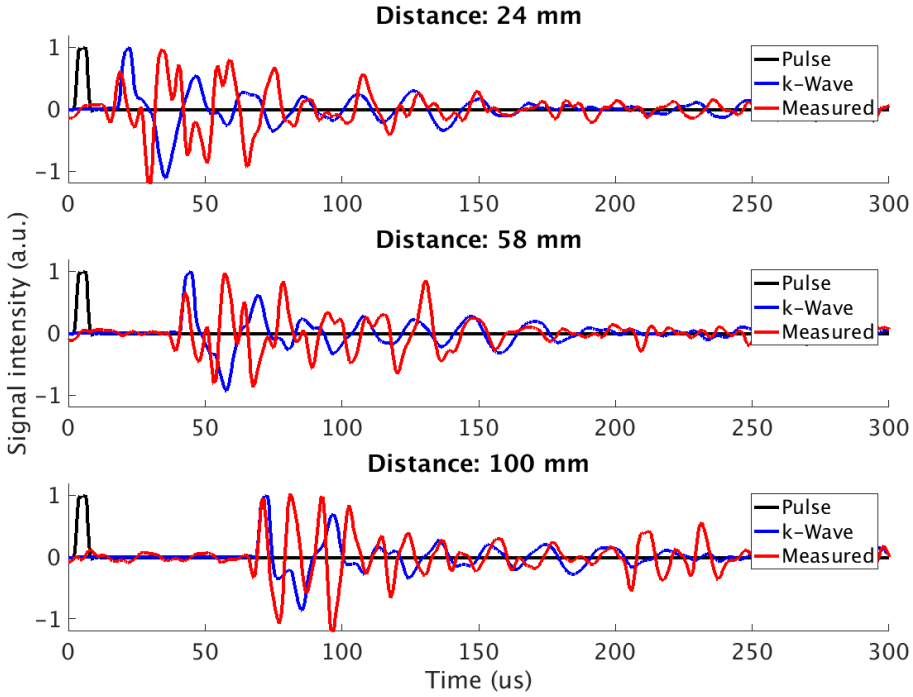

Figure 6. Unfiltered measured (red) and simulated (blue) acoustic signals at three different lead block to transducer distances. In black, measured dose pulse. Data taken with Truebeam unit.

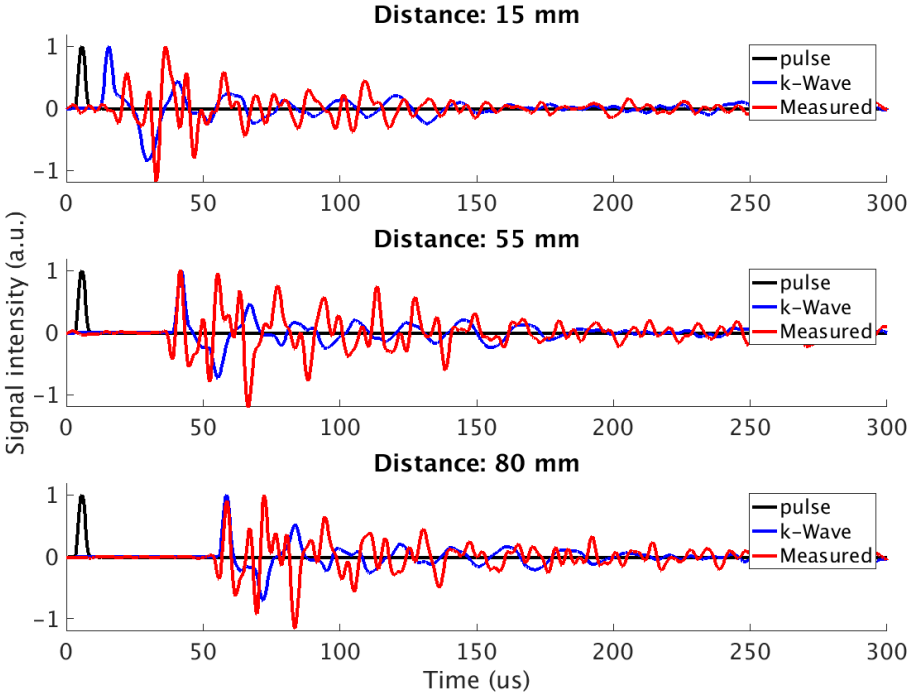

Figure 7. Unfiltered measured (red) and simulated (blue) acoustic signals at three different lead block to transducer distances. In black, measured dose pulse. Data taken with the Cyberknife unit.

3.3. Estimating the frequency response of the system

While the arrival times and pulse durations of the signals are in good agreement between measurement and simulation, the shape of the waves is still not well-reproduced, with certain high-frequency components seen in the measurements that cannot be reproduced by the simulations (Caballero *et al* 2013). This is caused by the fact that the frequency response of the detection system, composed of the transducer and the amplifiers, is not taken into account in the simulation. In order to improve the model of the system, we performed a spectral analysis of the measured and simulated curves from the Cyberknife unit, with a lead block to transducer signal of 80 mm, after filtering out the electromagnetic noise and correcting for detection delay. Then, we performed a Fourier analysis of the two signals and created a complex filter by dividing them in the frequency domain. This filter represents the frequency response of the system. The two spectra and the obtained filter are shown in Figure 8.

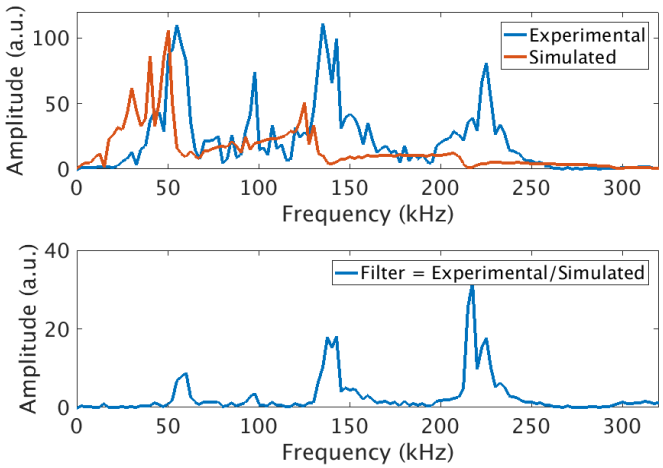

Figure 8. (Top) Fourier analysis of the Cyberknife-80 mm measured and simulated signal. (Bottom) Filter representing frequency response of the system.

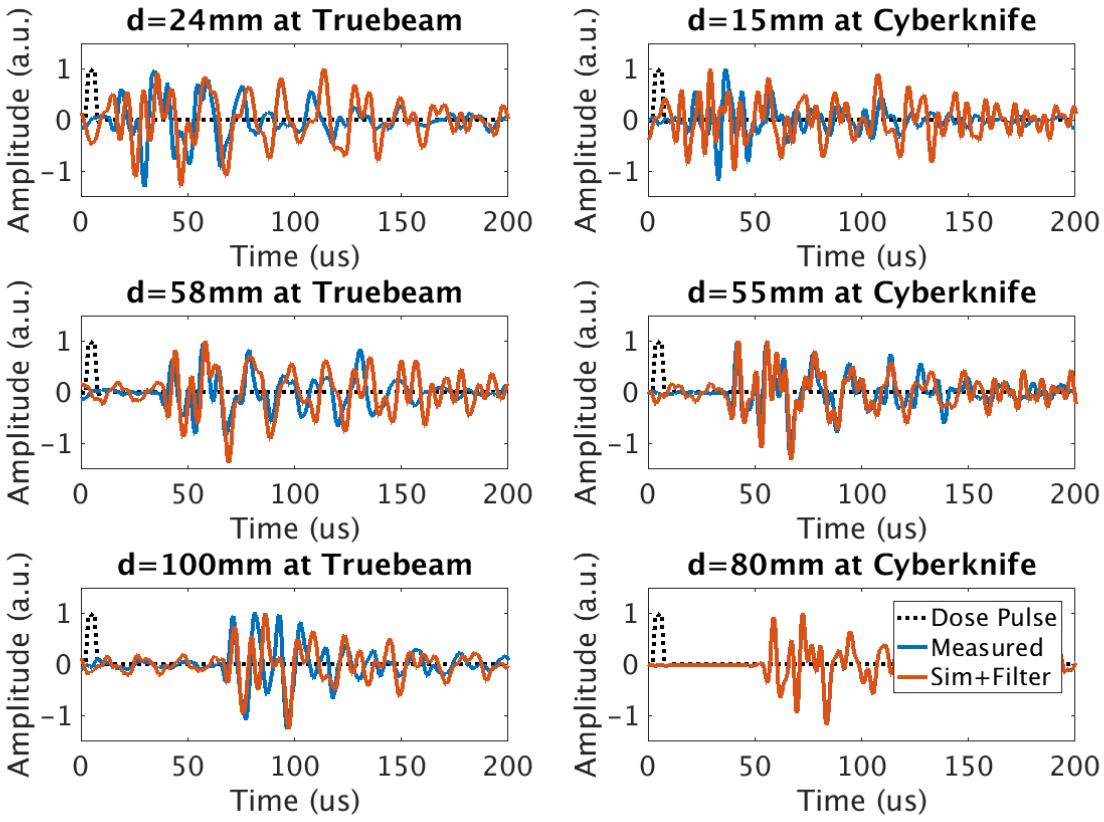

Figure 9. Results of applying the frequency response filter (Figure 7) to the simulated signals in the Truebeam and Cyberknife units (red), compared to measured signals (blue). Note that, by construction, the simulated+filter of the case d=80mm with the Cyberknife matches perfectly the measured data.

As seen in Figure 9, the application of the response filter significantly increases agreement between experiment and simulation in the clean area (above 55 mm lead block to transducer distance). The frequency response estimated from Cyberknife measurements was successfully applied to measurements in the Truebeam accelerator.

4. Discussion and conclusions

The proposed setup can detect acoustic waves originated from dose with µs-long pulses. As shown by other authors (Xiang et al 2013b, Hickling *et al* 2014a), lead amplification can increase detection limits and facilitate the developing and testing of detector setups. While the thermal noise at the transducer should not limit the accuracy of the system significantly (Ahmad *et al* 2015), the presence of strong electromagnetic and radiofrequency fields in a radiotherapy treatment room makes it necessary to use very low noise electronics (Diao *et al* 2015, Jones *et al* 2015), characterize thoroughly the background signals associated with the acceleration of the beam to perform a dry run for background subtraction (Hickling *et al* 2018a) and average a high number of samples to isolate the acoustic signal. In an environment with high levels of electromagnetic noise, digital treatment of the signals and noise subtraction techniques are vital for a successful measurement. In this context, the possibility to perform 'dry' runs to estimate the electromagnetic background synchronized with the dose pulse is extremely useful to obtain a clear photoacoustic signal since, when monitoring real patient treatments, the number of averaged samples is limited by the dose prescribed to the patient. In this context, the obtained SNR after 1000 samples are enough to filter out all random noise from the detected waves, where the dose deposited (assuming 100% pulse collection efficiency) is in the order of 0.5 Gy at the point of maximum dose, compatible with a 2-Gy fraction in the planning target volume of a clinical treatment. Also, the measurements shown were performed at room temperature; at body temperature, the intensity of protoacoustic waves would increase (Sulak *et al* 1979), which would improve the results.

While the proposed setup is similar to the suggested in previous works (Diao *et al* 2015, Hickling et al 2014, 2017), the post-processing of the signals (background subtraction in dry run + filter by frequency response of the system) is novel and allows for a cleaner measurement of the acoustic waves. In systems where this dry run mode is not available, it could be achieved by delivering the radiation fields with the jaws closed or away from the volume of interest. The simulation package composed by FLUKA + k-Wave + frequency response filter has performed well: the calculated signals reproduce successfully the arrival times and pulse shapes for the first 150 μs of the signals, provided that the detector is placed at sufficient distance (>50 mm) from the origin of the wave front; future measurements should aim at establishing this distance with higher accuracy. The description of the system response by a complex filter makes it harder to derive a physical interpretation of the system behavior from it: the intrinsic mechanical complexity of the transducer, added to the contribution of the amplification and filtering electronics, create a combination of frequency-dependent delays and amplitude changes that cannot be represented by a real filter. The problem is increased by the fact that we are working out of the transducer pass-band, which should be improved in the future by designing a specific transducer matched to the expected acoustic frequency content of the pressure wave. However, the model could successfully be applied in different irradiation conditions yielding coherent and repeatable results.

By separating the variations in the acoustic waveform caused by detector response and geometrical distribution of the initial pressure wave, we could use the latter to perform a three-dimensional reconstruction of the initial dose maps from the detected waves using the XACT technique (Hickling *et al* 2014b, 2018a, Lei *et al* 2018). However, while present implementations of XACT have used relatively simple filtered back-projection (FBP) methods to derive the dose distribution, a full understanding of the geometrical pressure wave can facilitate the use of more sophisticated methods, such as Full Wave Inversion or FWI (Pérez-Liva et al 2017), to significantly improve reconstruction efficiency.

Further developments of thermoacoustic detectors for radiation, including in-vivo dosimetry and image reconstruction from clinical photon and proton beams, are expected in the future. For instance, the comparison of repeated measurements taken at different treatment fractions can be used to identify interfractional organ motion affecting dose conformity, in a similar fashion as performed by some treatment centers with regard to PET distribution after irradiation (Bauer *et al* 2013). Also, the presented measurements are of interest for groups working on protoacoustic range verification, as we show that photon beams can be used as a test bench, given their wider availability and more favorable properties of the temporal pulse.

Acknowledgements

Work supported by the Spanish Government (FPA2015-65035-P, RTC-2015-3772-1), Comunidad de Madrid (S2013/MIT-3024 TOPUS-CM) and European Regional Funds. This is a contribution for the Moncloa Campus of International Excellence, “Grupo de Física Nuclear-UCM”, Ref. 910059. The authors want to thank the service of Medical Physics of Hospital Ruber Internacional, especially Francisco Fayos and Elena Antolín, for their support and assistance during the experiments, as well as the protoacoustics team at UPenn (Kevin Jones, Wei Nie, Ali Kassaee) for their help and valuable discussions.

References

Ahmad, M., Xiang, L., Yousefi, S., & Xing, L. (2015). Theoretical detection threshold of the proton-acoustic range verification technique. Medical physics, 42(10), 5735-5744.

Albul, V. I., Bychkov, V. B., Gusev, K. E., Demidov, V. S., Demidova, E. V., Konovalov, S. L., ... & Rostovtsev, A. A. (2001). Measurements of the parameters of the acoustic radiation accompanying the moderation of an intense proton beam in water. Instruments and Experimental Techniques, 44(3), 327-334.

Alsanea, F., Moskvin, V., & Stantz, K. M. (2015). Feasibility of RACT for 3D dose measurement and range verification in a water phantom. *Medical physics*, *42*(2), 937-946.

Assmann, W., Kellnberger, S., Reinhardt, S., Lehrack, S., Edlich, A., Thirolf, P. G., ... & Parodi, K. (2015). Ionoacoustic characterization of the proton Bragg peak with submillimeter accuracy. *Medical physics*, *42*(2), 567-574.

Bauer, J., Unholtz, D., Sommerer, F., Kurz, C., Haberer, T., Herfarth, K., ... & Parodi, K. (2013). Implementation and initial clinical experience of offline PET/CT-based verification of scanned carbon ion treatment. Radiotherapy and Oncology, 107(2), 218-226.

Beard, P. (2011). Biomedical photoacoustic imaging. Interface focus, rsfs20110028.

Böhlen, T. T., Cerutti, F., Chin, M. P. W., Fassò, A., Ferrari, A., Ortega, P. G., ... & Vlachoudis, V. (2014). The FLUKA code: developments and challenges for high energy and medical applications. Nuclear data sheets, 120, 211-214.

Caballero, M. A. A., Rosenthal, A., Buehler, A., Razansky, D., & Ntziachristos, V. (2013). Optoacoustic determination of spatio-temporal responses of ultrasound sensors. IEEE transactions on ultrasonics, ferroelectrics, and frequency control, 60(6), 1234-1244.

Diao, X., Zhu, J., Li, W., Deng, N., Chin, C. T., Zheng, X., ... & Kuang, Y. (2015). Broadband detection of dynamic acoustic emission process induced by 6 MV therapeutic X-ray beam from a clinical linear accelerator. In Ultrasonics Symposium (IUS), 2015 IEEE International (pp. 1-4). IEEE.

Ferrari, A., Sala, P. R., Fasso, A., & Ranft, J. (2005). FLUKA: A multi-particle transport code (Program version 2005) (No. INFN-TC-05-11).

Fontanarosa, D., Meer, S., Harris, E., & Verhaegen, F. (2011). A CT based correction method for speed of sound aberration for ultrasound based image guided radiotherapy. *Medical physics*, *38*(5), 2665-2673.

Fraile, L.M., Mach, H., Vedia, V., Olaizola, B., Paziy, V., Picado, E. & Udías, J.M., 2013. Fast timing study of a $CeBr_3$ crystal: Time resolution below 120 ps at ^{60}Co energies. *Nucl. Instrum. Methods A* 701, 235-242.

Giza O.M. 2017. Estudio de optimización del montaje experimental para mediciones gammaacústicas. *MSc. Thesis,* Universidad Complutense de Madrid. Available at http://nuclear.fis.ucm.es

Hayakawa, Y., Tada, J., Inada, T., Kitagawa, T., Wagai, T., & Yosioka, K. (1988). Acoustic pulse generation in excised muscle by pulsed proton beam irradiation and the possibility of clinical application to radiation therapy. *Journal of the Acoustical Society of Japan (E)*, *9*(5), 255-257.

Hayakawa, Y., Tada, J., Arai, N., Hosono, K., Sato, M., Wagai, T., ... & Tsujii, H. (1995). Acoustic pulse generated in a patient during treatment by pulsed proton radiation beam. Radiation Oncology Investigations, 3(1), 42-45.

Haynes, W. M. (Ed.). (2014). *CRC handbook of chemistry and physics*. CRC press.

Hickling, S., Léger, P., & El Naqa, I. (2014a). Simulation and experimental detection of radiation-induced acoustic waves from a radiotherapy linear accelerator. In *Ultrasonics Symposium (IUS), 2014 IEEE International* (pp. 29-32). IEEE.

Hickling, S., Hobson, M., & El Naqa, I. (2014b). Feasibility of x-ray acoustic computed tomography as a tool for noninvasive volumetric in vivo dosimetry. International Journal of Radiation Oncology• Biology• Physics, 90(1), S843

Hickling, S., Lei, H., Hobson, M., Léger, P., Wang, X., & El Naqa, I. (2017). Experimental evaluation of x-ray acoustic computed tomography for radiotherapy dosimetry applications. *Medical physics*, *44*(2), 608-617.

Hickling, S., Hobson, M., & El Naqa, I. (2018a). Characterization of x-ray acoustic computed tomography for applications in radiotherapy dosimetry. IEEE Transactions on Radiation and Plasma Medical Sciences.

Hickling, S., Xiang, L., Jones, K. C., Parodi, K., Assmann, W., Avery, S., ... & El Naqa, I. (2018b). Ionizing radiation-induced acoustics for radiotherapy and diagnostic radiology applications. *Medical physics, 14* (7), e707-e721.

PTCOG (2018), Particle therapy facilities in operation (last update: April 2018). Particle Therapy Co-Operative Group (PTCOG), www.ptcog.ch

Jones, K. C., Witztum, A., Sehgal, C. M., & Avery, S. (2014). Proton beam characterization by proton-induced acoustic emission: simulation studies. Physics in Medicine & Biology, 59(21), 6549.

Jones, K. C., Vander Stappen, F., Bawiec, C. R., Janssens, G., Lewin, P. A., Prieels, D., ... & Avery, S. (2015). Experimental observation of acoustic emissions generated by a pulsed proton beam from a hospital-based clinical cyclotron. Medical physics, 42(12), 7090-7097.

Jones, K. C., Seghal, C. M., & Avery, S. (2016a). How proton pulse characteristics influence protoacoustic determination of proton-beam range: simulation studies. Physics in Medicine & Biology, 61(6), 2213.

Jones, K. C., Vander Stappen, F., Sehgal, C. M., & Avery, S. (2016b). Acoustic time-of-flight for proton range verification in water. Medical physics, 43(9), 5213-5224.

Jones, K. C., Nie, W., Chu, J. C., Turian, J. V., Kassaee, A., Sehgal, C. M., & Avery, S. (2018). Acoustic-based proton range verification in heterogeneous tissue: simulation studies. Physics in Medicine & Biology, 63(2), 025018.

Kim, J., Park, E. Y., Jung, Y., Kim, B. C., Kim, J. H., Yi, C. Y., ... & Kim, C. (2017). X-Ray Acoustic-Based Dosimetry Using a Focused Ultrasound Transducer and a Medical Linear Accelerator. *IEEE Transactions on Radiation and Plasma Medical Sciences*, *1*(6), 534-540.

Kipergil, E. A., Erkol, H., Kaya, S., Gulsen, G., & Unlu, M. B. (2017). An analysis of beam parameters on proton-acoustic waves through an analytic approach. Physics in Medicine & Biology, 62(12), 4694.

Lei, H., Zhang, W., Oraiqat, I., Liu, Z., Ni, J., Wang, X., & El Naqa, I. (2018). Toward in vivo dosimetry in external beam radiotherapy using x-ray acoustic computed tomography: A soft-tissue phantom study validation. Medical physics, 45(9), 4191-4200.

Lehrack, S., Assmann, W., Bertrand, D., Henrotin, S., Herault, J., Heymans, V., ... & &, K. (2017). Submillimeter

ionoacoustic range determination for protons in water at a clinical synchrocyclotron. *Physics in Medicine & Biology*, *62*(17), L20.

Lyamshev L.M., (2014) *Radiation Acoustics*. Boca Raton, FL, USA: CRC Press

Nie, W., Jones, K. C., Petro, S., Kassaee, A., Sehgal, C. M., & Avery, S. (2018). Proton range verification in homogeneous materials through acoustic measurements. Physics in Medicine & Biology, 63(2), 025036.

Paganetti, H. (2012). Range uncertainties in proton therapy and the role of Monte Carlo simulations. Physics in Medicine & Biology, 57(11), R99.

Parodi, K., & Assmann, W. (2015). Ionoacoustics: A new direct method for range verification. *Modern Physics Letters A*, *30*(17), 1540025.

Patch, S. K., Santiago-Gonzalez, D., & Mustapha, B. (2019). Thermoacoustic range verification in the presence of acoustic heterogeneity and soundspeed errors–Robustness relative to ultrasound image of underlying anatomy. Medical physics 46 (1), 318-327.

Pérez-Liva, M., Herraiz, J. L., Udías, J. M., Miller, E., Cox, B. T., & Treeby, B. E. (2017). Time domain reconstruction of sound speed and attenuation in ultrasound computed tomography using full wave inversion. The Journal of the Acoustical Society of America, 141(3), 1595-1604.

Sampaio, D. R., Uliana, J. H., Carneiro, A. A., Pavoni, J. F., Pavan, T. Z., & Borges, L. F. (2015, October). X-ray acoustic imaging for external beam radiation therapy dosimetry using a commercial ultrasound scanner. In *Ultrasonics Symposium (IUS), 2015 IEEE International* (pp. 1-4). IEEE.

Sánchez-Tembleque V., Sánchez-Parcerisa D., Fraile L.M., Udías J., 2018. Simultaneous measurement of the spectral and temporal properties of a LINAC pulse from outside the treatment room. *Rad. Phys. Chem.* [submitted]

Sieger, G. E., & Lefevre, H. W. (1985). Time-resolved measurement of acoustic pulses generated by MeV protons stopping in aluminum. *Physical Review A*, *31*(6), 3929.

Sulak, L., Armstrong, T., Baranger, H., Bregman, M., Levi, M., Mael, D., ... & Bradner, H. (1979). Experimental studies of the acoustic signature of proton beams traversing fluid media. *Nuclear Instruments and Methods*, *161*(2), 203-217.

Treeby, B. E., Zhang, E. Z., & Cox, B. T. (2010). Photoacoustic tomography in absorbing acoustic media using time reversal. *Inverse Problems*, *26*(11), 115003.

Vedia, V., Mach, H., Fraile L.M., Udías, J.M. & Lalkovski, S., 2015. Enhanced time response of 1-in. $LaBr_3$(Ce) crystals by leading edge and constant fraction techniques. *Nucl. Instrum. Methods A* 795, 244-50.

Xiang, L., Han, B., Carpenter, C., Pratx, G., Kuang, Y., & Xing, L. (2013a). X-ray induced photoacoustic tomography. In *Photons Plus Ultrasound: Imaging and Sensing 2013* (Vol. 8581, p. 85811I). International Society for Optics and Photonics.

Xiang, L., Han, B., Carpenter, C., Pratx, G., Kuang, Y., & Xing, L. (2013b). X-ray acoustic computed tomography with pulsed x-ray beam from a medical linear accelerator. *Medical physics*, *40*(1).